



Trans. Nonferrous Met. Soc. China 31(2021) 1350-1362

Transactions of Nonferrous Metals Society of China

www.tnmsc.cn



# Effect of Zr content on crack formation and mechanical properties of IN738LC processed by selective laser melting

Yong HU<sup>1,2</sup>, Xiao-kang YANG<sup>1,2</sup>, Wen-jiang KANG<sup>1,2</sup>, Yu-tian DING<sup>1,2</sup>, Jia-yu XU<sup>1,2</sup>, Hui-ying ZHANG<sup>1,2</sup>

- 1. State Key Laboratory of Advanced Processing and Recycling of Non-ferrous Metals, Lanzhou University of Technology, Lanzhou 730050, China;
- 2. School of Materials Science and Engineering, Lanzhou University of Technology, Lanzhou 730050, China

Received 12 June 2020; accepted 22 December 2020

**Abstract:** Two batches of commercial IN738LC alloy powders with different Zr contents were printed under the same parameters. The influences of Zr content (0.024 wt.% and 0.12 wt.%, respectively) in powders on crack density, distribution, formation mechanism and mechanical properties of selective laser melting (SLM)-treated parts were systematically studied. It was found that the crack density (area ratio) increases from 0.15% to 0.87% in the *XOY* plane and from 0.21% to 1.81% in the *XOZ* plane along with the Zr content increase from 0.024 wt.% to 0.12 wt.% in the original powders. Solidification cracks are formed along the epitaxially grown (001)-oriented columnar grain boundaries in molten pool center. The ultimate tensile strength of Sample 1 (0.024 wt.% Zr) is 1113 MPa, and there are dimples in tensile fracture. With an increase in the Zr content to 0.12 wt.% (Sample 2), the ultimate tensile strength of Sample 2 decreases to 610 MPa, and there are numerous original cracks and exposed columnar grain boundaries in tensile fracture. The optimization of printing parameters of Sample 2 considerably increases the ultimate tensile strength by 55.2% to 947 MPa, and the plasticity is greatly improved.

**Key words:** selective laser melting; IN738LC alloy; Zr content; solidification crack; process parameter optimization; mechanical properties

#### 1 Introduction

Selective laser melting (SLM) technology can realize the formation of various refractory and difficult-to-process materials owing to its small laser spot diameter and energy concentration characteristics. The processing procedure does not require a mold and allows the direct preparation of complex shapes [1]. Currently, SLM technology is widely used to process numerous metal and alloy materials such as aluminum, titanium, nickel, and iron [2–5].

It is determined that both the print processing parameters and properties of powders considerably affect the crack formation and the mechanical properties. IN738LC is a nickel-based superalloy strengthened by  $\gamma'$  (Ni<sub>3</sub> (Al,Ti)) phase precipitation, which has an excellent creep strength and corrosion resistance and acts as a popular material for gas turbine blades and valves [6,7]. However, the total content of Al and Ti is greater than 6.5 wt.% in the precipitation strengthening  $\gamma'$  (Ni<sub>3</sub>(Al,Ti)) phase, which results in high crack sensitivity and restricts the properties of SLM-treated IN738LC alloy [8,9].

So far, researchers have conducted many studies to improve the quality of SLM parts. GU et al [10] have studied the relationship among powder characteristics, forming parameters, and part properties of the Ti-6Al-4V alloy obtained from different suppliers. CARTER et al [11] and CATCHPOLE-SMITH et al [12] have identified an

effective mechanism between the scanning strategy and the formation as well as the distribution of cracks in CM247LC; the results showed that a favorable scanning strategy reduces the crack density and increases the compactness of the SLM-treated parts. WANG et al [13] pre-sieved the powder and adopted appropriate process parameters to print an almost completely dense and crack-free IN738LC alloy sample, which exhibited high strength and ductility under later HIP and dual aging heat treatment. The optimization of process parameters can improve the quality of parts, whereas a trace element content in the original powder of the same alloy causes instability in the SLM forming process and quality. Meanwhile, printing parameters corresponding to various trace element content powders are also changed, which affects the production cost and efficiency.

As reported by ENGELI et al [14], a small change in the Si content in powder material will considerably affect the cracking sensitivity and final micro-crack density of the IN738LC alloy. TOMUS et al [15] have indicated that crack initiation is mainly induced during solidification, and lower Si and C total content is conducive to suppressing cracks in the Hastelloy-X alloy. The addition of Zr to superalloys reduces grain boundary defects, improves grain boundary binding force, and decreases the rate of grain boundary diffusion. Meanwhile, Zr segregation at the grain boundary decreases the interface energy and the grain size, alters the morphology of the grain boundary phase, reduces the total content of S and C in the alloy, improves ductility, and eliminates notch sensitivity. However, it has been shown that excessive Zr content considerably affects the cracking sensitivity during casting and welding [16-18]. HEYDARI et al [19] have studied the effect of trace Zr content (0.01-0.04 wt.%) on the hot cracking of as-cast IN738LC alloy turbine blades; it was determined that the grain size and secondary dendrite arm spacing did not considerably affect the hot tear. With an increase in the Zr content, there was a clear increase in hot cracking, which was attributed to eutectic development and its diffusion along the grain boundaries. Hot tearing in polycrystalline IN738LC was considerably suppressed by a decrease in the Zr content to 0.02 wt.%. LIANG et al [20] proposed a theoretical model for the segregation of micro-elements in a high-energy beam rapid directional solidification multicomponent alloy. Furthermore, CLOOTS et al [21] concluded that the enrichment of Zr forms a low-melting-point phase, which results in the emergence of solidification cracks in the IN738LC alloy. However, the effect of content of trace Zr element in the original powder on the SLM solidification process require an in-depth research.

Therefore, in this research, the crack density, distribution, formation mechanism and mechanical properties of two batches of powders during the SLM forming process were systematically studied. These results will help in understanding the effect of trace elements in original powder on the printing quality and their interaction with process parameters.

#### 2 Experimental

#### 2.1 Materials

Commercial IN738LC alloy powders used herein were purchased from two different powder suppliers; both batches of powders were prepared through argon atomization. Powder particles are predominantly spherical or spheroidal; some particles are ellipsoidal or dumbbell-shaped (Fig. 1). Batch 1# powders (Sample 1, Fig. 1(a)) have many satellite powders on the powder surface, whereas batch 2# powders (Sample 2, Fig. 1(b)) have relatively smooth surfaces. The particle size of the two batches of powders is within the range of 10-53 μm, and their particle size distribution is similar. The compositions of these powders were detected using inductively coupled plasma mass spectrometry (ICP-MS) and infrared absorption spectroscopy (for light elements such as O and C). Zr content in Sample 2 is five times that of Sample 1 (Table 1). The physical properties of the two batches of powders are shown in Table 2. Both batches of powders have similar median particle size  $D_{50}$ , apparent density, and tap density; Sample 2 has better fluidity than Sample 1 owing to its better surface quality and relatively independent particles.

#### 2.2 Methods

SLM-treated cubic samples ( $10 \text{ mm} \times 10 \text{ mm} \times 10 \text{ mm}$ ) and tensile samples corresponding to two batches of powders are defined as Sample 1 (0.024 wt.% Zr) and Sample 2 (0.12 wt.% Zr),

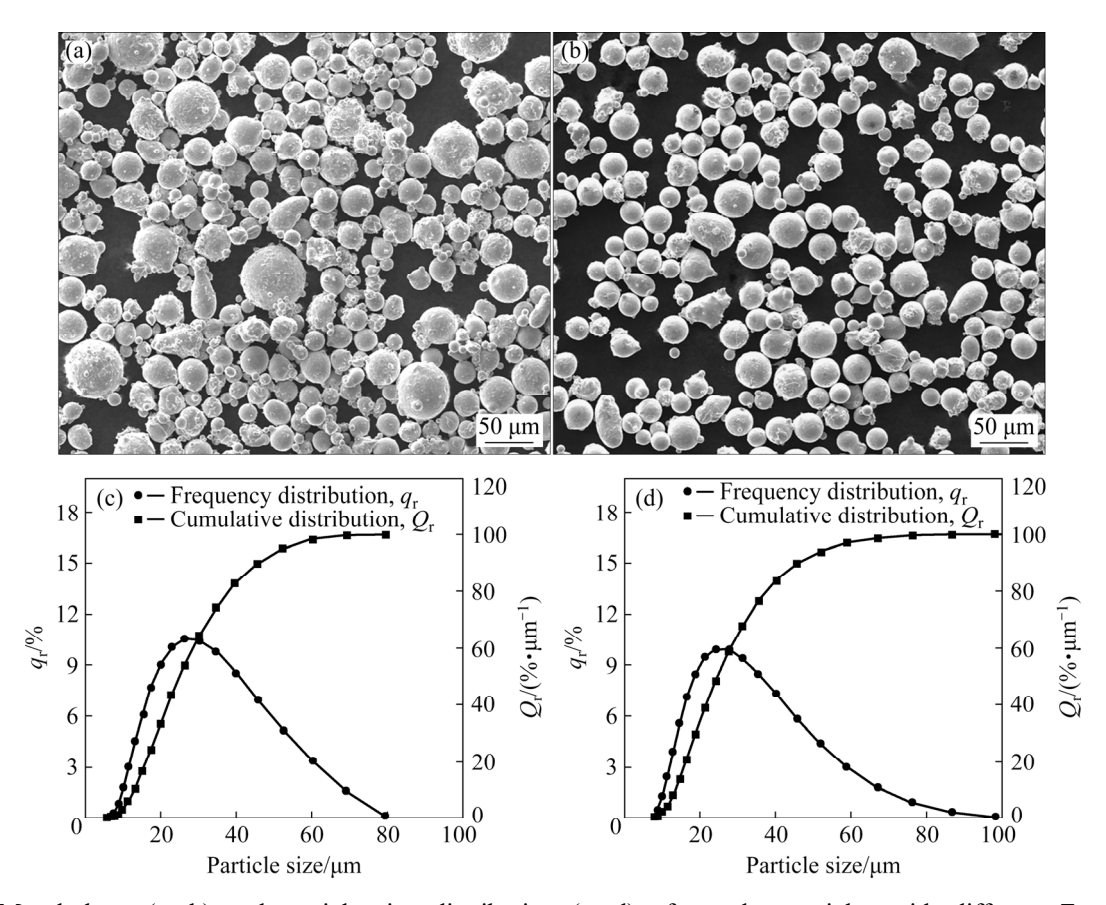


**Fig. 1** Morphology (a, b) and particle size distribution (c, d) of powder particles with different Zr contents: (a, c) Sample 1; (b, d) Sample 2

**Table 1** Chemical compositions of IN738LC alloy powders (wt.%)

		1	<i>J</i> 1					
	Sample	Cr	Co	Al	Ti	W	Mo	Та
	Sample 1	15.88	8.40	3.50	3.42	2.48	1.70	1.67
	Sample 2	15.74	8.47	3.44	3.28	2.64	1.84	1.85
	IN738LC [22]	15.7-16.3	8.00-9.00	3.2-3.7	3.2-3.7	2.4-2.8	1.54-2.0	1.5-2.0
	Sample	С	В	Nb	Zr	Si	О	Ni
	Sample 1	0.10	0.011	0.86	0.024	0.030	0.018	Bal.
	Sample 2	0.12	0.012	0.91	0.120	0.040	0.014	Bal.
	IN738LC [22]	0.15-0.20	0.005-0.015	0.6-1.1	0.05-015	≤0.30	_	Bal.

**Table 2** Physical properties of powders

Sample No.	Sample No. $D_{10}/\mu m$		$D_{90}/\mu\mathrm{m}$	Flow ability/ $(s \cdot (50g)^{-1})$	Apparent density/ (g·cm <sup>-3</sup> )	Tap density/ (g·cm <sup>-3</sup> )
1	14.96	28.72	52.90	23.40	4.20	5.04
2	15.10	27.90	52.90	19.00	4.14	4.96

respectively. EOSINT M280, equipped with a Yb fiber laser and the spot diameter of 0.1 mm, was used to fabricate the samples. Alloy powders were kept in a vacuum drying box at 150 °C for 4 h; then, samples were printed on a 100 °C preheated 304

stainless steel substrate (250 mm × 250 mm) under an argon atmosphere. To visually investigate the cross-section morphology of molten pool and internal growth microstructure, based on the orthogonal experiment, the following printing

process parameters are determined [23]: laser power of 270 W, scanning speed of 1150 mm/s, hatch distance of 0.09 mm, layer thickness of 0.04 mm, and an inter-laminar rotation of 90°. The scanning strategy of 67° between layers and the optimized process parameters were chosen to compare the mechanical properties of tensile specimens.

Subsequent to mechanical grinding and polishing the samples, five images of *XOY* and *XOZ* surfaces of each sample at the same magnification were acquired using optical microscopy from random locations. Then, the proportion of crack areas in each plane and the average crack density in the corresponding plane were calculated using the Image Pro-plus software. Metallographic samples were corroded in a 10 mL HNO<sub>3</sub> + 30 mL HCl mixed solution for 30 s to observe the crack formation locations and crack morphologies of *XOY* and *XOZ* planes. The microstructure and grain orientation were characterized and analyzed

through a Quanta FEG 450 thermal field emission scanning electron microscopy instrument equipped with an electron backscattered diffraction system. The microscopic morphology and elemental distribution of samples were detected with an FEI TecnaiG2 TEM transmission electron microscopy instrument, which was equipped with an energy dispersive X-ray spectroscopy (EDX) attachment and operated at an accelerating voltage of 200 kV. The samples were electrolytically double jet thinned in an electrolyte containing 10% perchloric acid and 90% ethanol. The AGS-X electronic universal material testing machine was utilized to test the tensile properties of SLM-treated samples.

#### 3 Results

#### 3.1 Crack density

Figure 2 shows the optical micrographs of SLM-treated cubic samples having different Zr

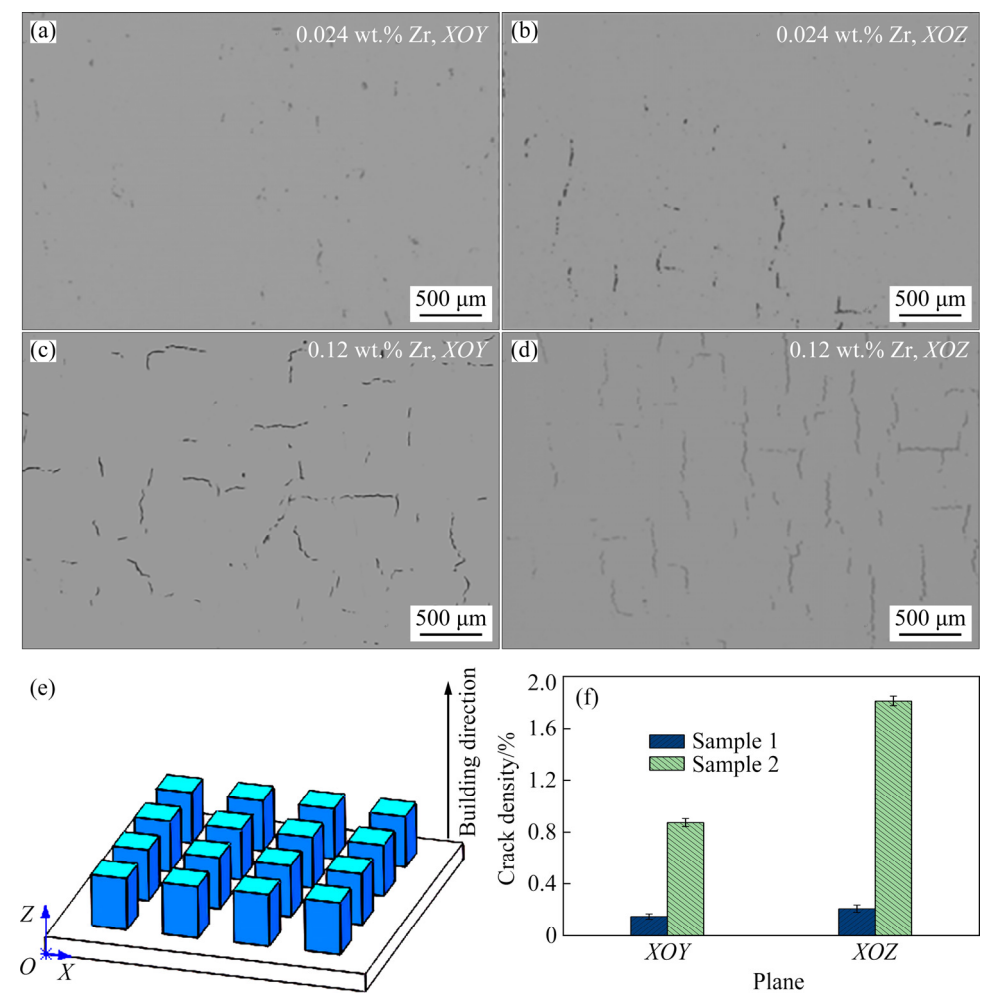


**Fig. 2** Crack morphology and crack density of SLM-treated samples with different Zr contents: (a, b) Crack distribution of Sample 1; (c, d) Crack distribution of Sample 2; (e) Schematic diagram of SLM building direction; (f) Crack density histogram of Sample 1 and Sample 2

contents. The crack density and distribution are considerably sparser in the XOY and XOZ planes of Sample 1 (0.024 wt.% Zr) (Figs. 2(a) and (b)) compared with those in Sample 2 (0.12 wt.% Zr) (Figs. 2(c) and (d)). The cracks in both samples show irregular extension and limited length in the printing plane (XOY). Most cracks in the XOZ plane extend along the Z axis (building direction (see Fig. 2(e))), and their length clearly increases and penetrates into multiple layers. The crack density (area ratio) is approximately 0.15% (XOY) and 0.21% (XOZ) in Sample 1 (0.024 wt.% Zr), whereas it is approximately 0.87% (XOY) and 1.81% (XOZ) in Sample 2 (0.12 wt.% Zr). In addition, two samples have the same forming process parameters and experience similar thermal cycling and thermal stress; however, the crack density in planes is quite different for a specific Zr content, as shown in Fig. 2(f).

#### 3.2 Crack formation location and morphology

The metallographic images of samples with different Zr contents are shown in Fig. 3. All samples in the *XOY* plane exhibit typical "checkerboard" characteristics, i.e., cracks are mainly distributed and spread along the checkerboard edges (Figs. 3(a) and (c)). In the *XOZ* 

plane, the cross-section of the U-shaped molten pool has a typical "fish-scale" feature; the cracks are concentrated inside molten pool and propagate through multiple layers in a long straight form, especially for Sample 2 (Fig. 3(d)).

The detailed morphology and distribution of cracks in the XOZ plane of Sample 2 (0.12 wt.% Zr) are shown in Fig. 4. The columnar crystals at the center of the molten pool epitaxially grow along the construction direction, which are marked by the red lines in Fig. 4(a). In addition, it is observed that cracks are mainly concentrated in these regions, and their lengths are several hundred of microns or even longer. The XOZ plane IPF map of Sample 2 in Fig. 4(b) shows that the oriented columnar crystals grow along the (100) direction, and the cracks extend to multiple layers along the growth direction of the columnar crystal. Figure 4(c) shows a high-magnification image of the red boxed area in Fig. 4(a), which shows that the interior of the molten pool is composed of columnar crystals grown in a random orientation. Owing to the effect of the printing process, crystals at the center of molten pool grow parallel to the construction direction, whereas the columnar crystals in the edge region of molten pool grow toward the center of the molten pool, and cracks occur in areas where

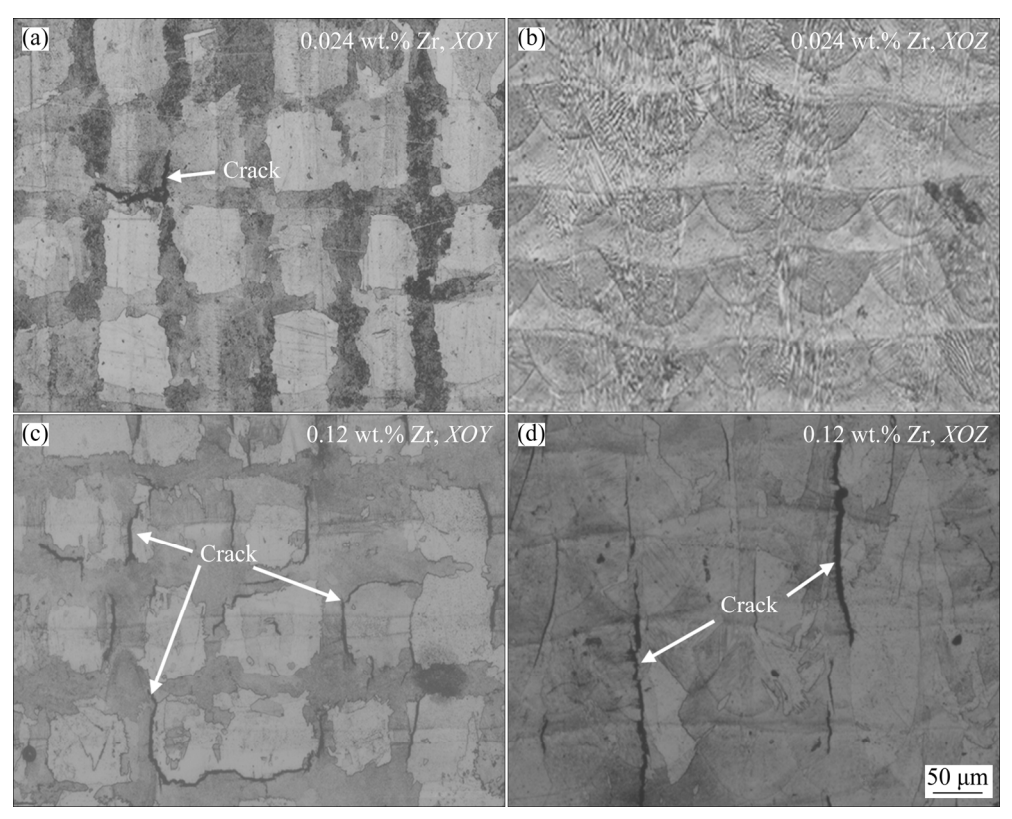


Fig. 3 Optical micrographs of Sample 1 (a, b) and Sample 2 (c, d) showing crack formation location

columnar crystals in two growth directions contact each other. Figure 4(d) shows a magnified image of the crack portion from the part indicated by the red arrow in Fig. 4(c). It is observed that the residual traces of liquid film exist at fracture grain boundaries.

## 3.3 Distribution of grain boundary phases and elements

Scanning transmission electron microscopy (STEM) images of samples with different Zr contents are shown in Fig. 5. There are many intertwined dislocations in grains and around the grain boundaries of two samples. A small number of near-spherical carbide particles with the size of

approximately 50 nm are distributed near the austenite grain boundary (Fig. 5(a)). With an increase in the Zr content to 0.12 wt.% (Fig. 5(b)), the size of carbide particles precipitated at austenite grain boundaries becomes approximately 100 nm; the number of carbide particles and the continuous distribution along grain boundaries considerably increase. Figures 6 and 7 show the EDX images of various elements in areas corresponding to the TEM bright field images of two samples (*XOY* plane). Figure 6 shows that when the Zr content is 0.024 wt.%, the distribution of each element is relatively uniform, Al is locally segregated, and Ti, Nb, Mo, and Zr are enriched in the position of precipitate particles. With an increase in the Zr

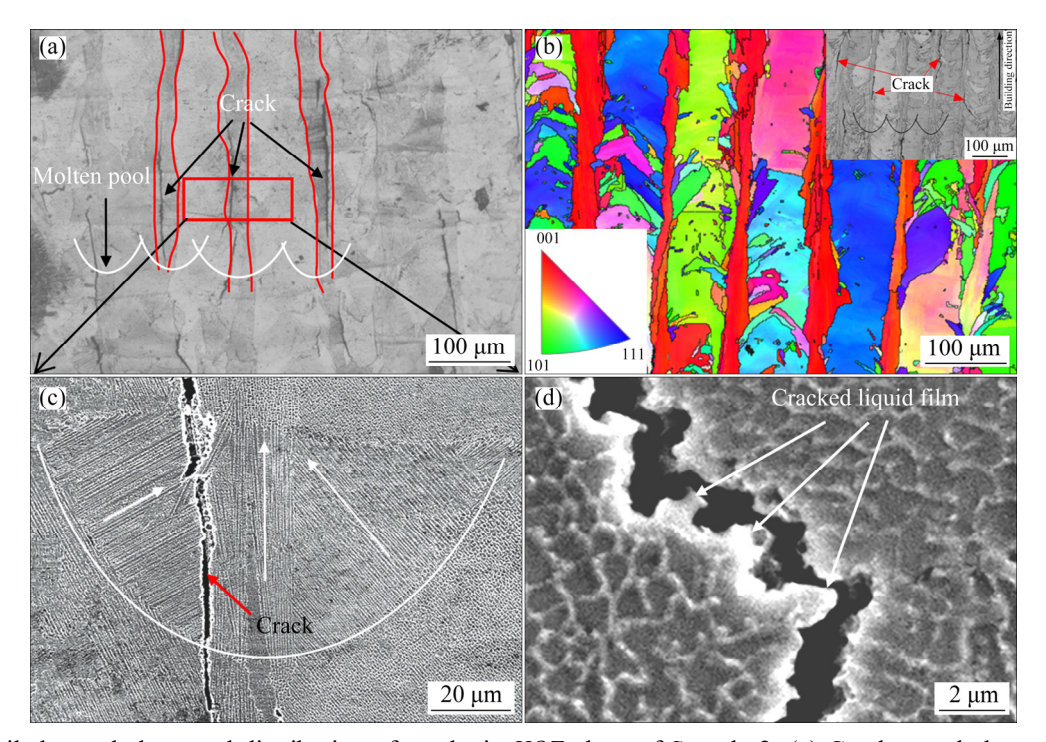


**Fig. 4** Detailed morphology and distribution of cracks in *XOZ* plane of Sample 2: (a) Crack morphology; (b) Inverse pole figure (IPF); (c) Typical molten pool section; (d) Residual traces of liquid film existing at fracture grain boundaries

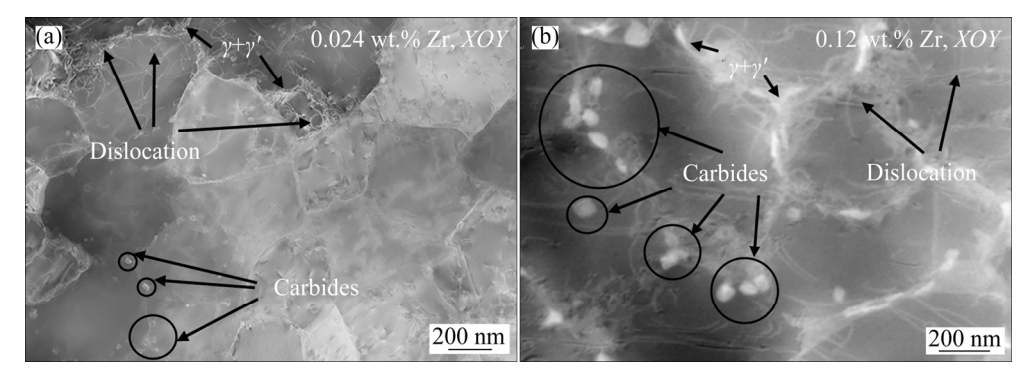


**Fig. 5** STEM images of SLM-treated samples with different Zr contents perpendicular to building direction: (a) Sample 1; (b) Sample 2

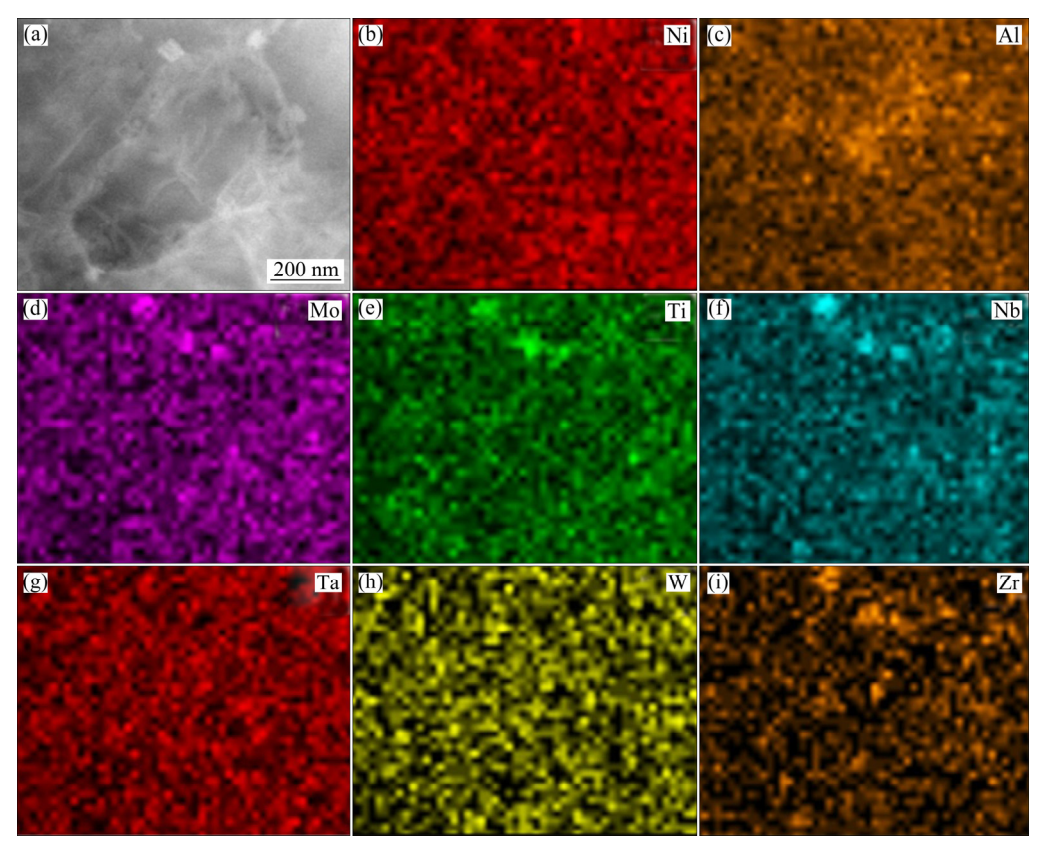


Fig. 6 TEM image (a) and elemental distributions (b-i) in XOY plane of Sample 1

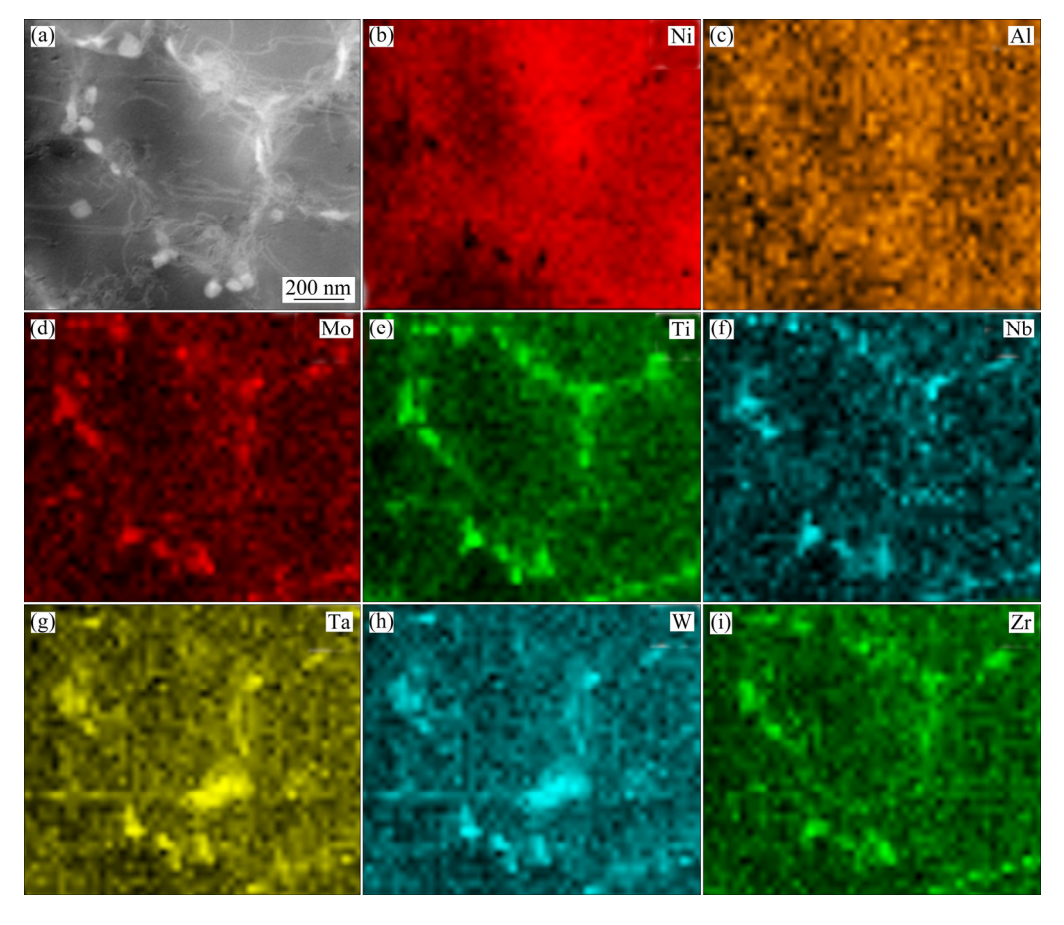
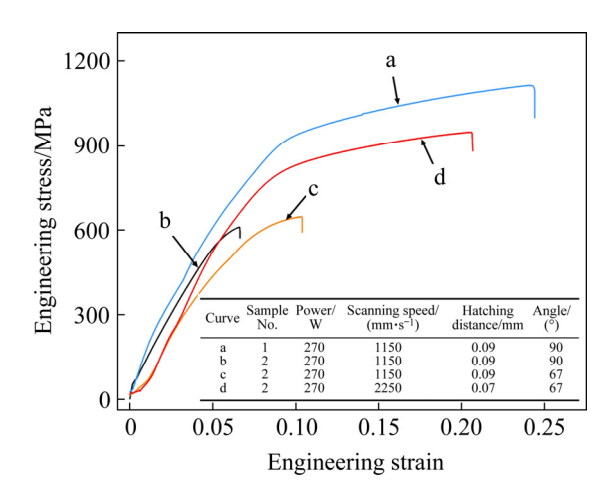


Fig. 7 TEM image (a) and elemental distributions (b-i) in XOY plane of Sample 2

content to 0.12 wt.%, as shown in Fig. 7, the enrichment of Ti, Nb, Ta, Mo, W, and Zr in particles distributed around grain boundaries is clearly strengthened, and the relative content of Al at grain boundaries is also higher than that in the grains.

#### 3.4 Mechanical properties

Figure 8 shows the tensile engineering stressstrain curves of samples prepared with different Zr contents at room temperature. Tensile samples were acquired from the XOY plane perpendicular to the building direction. Curve a in Fig. 8 corresponds to Sample 1 (0.024 wt.% Zr), which is under a yield strength of 930 MPa (the ultimate tensile strength reaches 1113 MPa) and exhibits good plasticity. Curve b corresponds to Sample 2 (0.12 wt.% Zr), and its ultimate tensile strength is only 610 MPa without a yielding phenomenon. corresponds to Sample 2 (0.12 wt.% Zr), whose laser interlayer scanning strategy is adjusted to 67°; its ultimate tensile strength increases to 647 MPa. By further optimizing the forming parameters of Sample 2 (0.12 wt.% Zr), the yield strength increases to 764 MPa, and the ultimate tensile strength considerably increases to 947 MPa, which is accompanied by an improved plasticity. The specific printing parameters samples corresponding to each curve are shown in the inset table in Fig. 8.



**Fig. 8** Engineering stress-strain curves of samples prepared from powders with different Zr contents at room temperature

#### 4 Discussion

The solidification structure and properties of SLM-treated parts are affected by the type of alloy

and processing parameters. In this study, identical processing parameters were applied to different batches of powders, which had the same alloy type. However, the solidification structure, crack density, and mechanical properties of samples were highly different owing to different trace Zr contents in the powders. Therefore, the effect of trace Zr content in original powders on the formation mechanism of solidification cracks and the quality of SLM-treated parts requires an in-depth investigation.

### 4.1 Solidification structure and crack formation mechanism

The solidification structure and the crack formation mechanism of typical SLM-treated molten pool were analyzed as follows. Subsequent to laser scanning, liquid metal in the molten pool transfers heat in the direction perpendicular to the boundary of the molten pool, and crystals grow against the temperature gradient toward the interior. For cubic metals, three preferred growth (001) orientations are perpendicular to each other. A change in the growth direction minimizes deflection angle between the maximum heat flow direction and preferred growth direction, which reduces resistance to crystal growth solidification [24]. As the heat dissipation direction is similar to the tectonic direction, columnar crystals located in the central regions of the molten pool preferentially grow, and solidification rate is greater than that in the edge regions [25]. In addition, the adoption of a 90° rotation scanning strategy between layers causes the N+1-layer molten metal to epitaxially grow, wherein columnar crystals with a (001) orientation at the center of the *N*-layer molten pool serve as nucleation points [26]. Finally, columnar crystals at the center of the molten pool penetrate the multiple deposition layers (Fig. 4(b)). In the edge region of the molten pool (Fig. 4(c)), columnar crystals grow gradually, and there are angle differences between growth and building directions, whereas the overall growth direction points toward the center of the molten pool [27]. When competitively grown central columnar crystals are in contact with edge columnar crystals, the pillar crystals stop growing, contact areas are solidified, and many insoluble elements are concentrated in the residual liquid phase, which forms a low-melting liquid film [28]. The solidification shrinkage of molten metal and high

temperature gradient in SLM forming make the molten pool subjected to tensile stress; once the tensile stress exceeds the critical liquid film breaking force [29], cracks will occur and extend to columnar grain boundaries [30]. The growth of column crystal and element enrichment at the boundaries are schematically shown in Fig. 9(a); the inner wall of cracks form an egg box-shaped bare columnar grain boundary morphology, as shown in Fig. 9(b), which agrees with typical solidification crack characteristics [31]. WOLF et al [32] and CLOOTS [21] have stated that solidification cracks are easy to form in deep melt pools; when the forming process parameters are adjusted to obtain a shallow melt pool, low-melting elements will transfer to the surface of the melt pool, and solidification cracks will be suppressed.

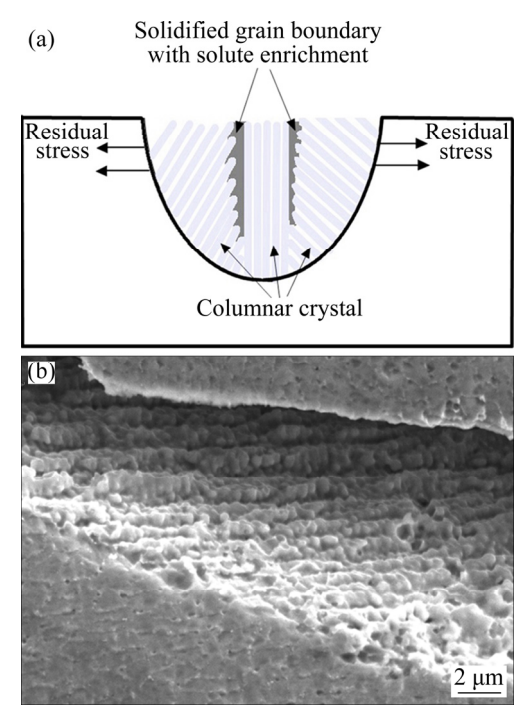
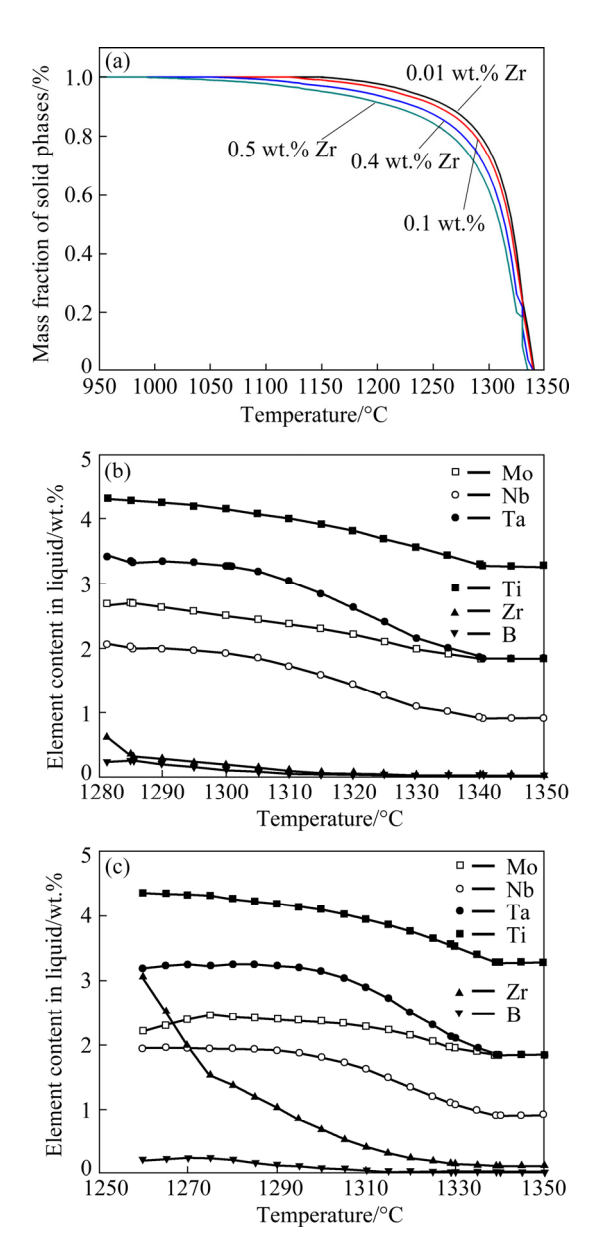


Fig. 9 Schematic diagram showing growth of column crystal and element enrichment at boundary (a) and morphology of inner wall of cracks (b)

#### 4.2 Effect of Zr on crack formation

During welding, the sensitivity of cracks was determined through metallurgical factors and the strain level at the end of solidification. The effect of residual stress resulting from solidification shrinkage and high temperature gradient on crack formation has been extensively confirmed. The adjustment of process parameters can suppress the occurrence of solidification cracks and improve the

quality of prints; different types and amounts of trace elements in the original powders also considerably affect the cracking sensitivity of the alloy. The solidification temperature range is affected by the redistribution of alloying elements during solidification and by the amount and existence of residual liquid at the interface [31]. To reveal the influence of metallurgical factors, a relationship between the Zr content in the IN738LC alloy and solidification temperature was determined using a non-equilibrium solidification calculation (Scheil–Gulliver model). The results are shown in Fig. 10(a). In Scheil–Gulliver model, it is assumed that the diffusion coefficient in the liquid phase is



**Fig. 10** Effect of Zr content on solidification temperature of IN738LC alloy (a), and element distributions in liquid during solidification for Sample 1 (b) and Sample 2 (c)

equal to infinity, and the diffusion coefficient in the solid phase is equal to zero. Local equilibrium is always maintained at the phase interface position between liquid and solid phases [33]. As shown in Fig. 10(a), when the Zr content increased from 0.01 wt.% to 0.5 wt.%, the final solidification temperature of alloy decreased from 1150 to 995 °C. Clearly, the solidus temperature of the alloy decreased, and the solidification temperature range increased from 190 to 345 °C. The variation trend of liquid element distribution during solidification with different Zr contents was simulated using the JMAT Pro software. Results show that the Zr content in the liquid phase of Sample 1 (0.024 wt.%) increases from 0.024 wt.% to the end of solidification of 0.63 wt.% (Fig. 10(b)), whereas the Zr content in the liquid phase of Sample 2 (0.12 wt.%) increases from 0.12 wt.% to the end of solidification of 3.05 wt.% (Fig. 10(c)). Therefore, an increase in the content of Zr in IN738LC alloy powders leads to a wider solidification temperature range. Columnar dendrites are solidified in a volume solidification mode, and the enriched Zr in the inter-dendritic liquid phase results in high sensitivity to solidification cracks in SLM-treated parts.

SLM technology exhibits high temperature gradient and rapid solidification characteristics. This technology can effectively reduce segregation of elements and form supersaturated solutions and solid metastable phases solidification process. However, the element distribution analyzed using TEM-EDX shows that Ti, Nb, Ta, Mo, W, Al, and Zr elements are enriched at the grain boundaries of Sample 2 (0.12 wt.% Zr) (Fig. 7), which is consistent with the calculated results of Fig. 10(c). The segregation of Ti, Nb, Ta, Mo, W, and Al elements was simultaneously promoted by the excessive Zr content. WANG et al [34] used the TEM-EDX analysis to study the SLM-treated nickel-based alloy CM247LC and determined that Ti, Al, Hf, Ta, and Cr elements were enriched in the precipitated particles at grain boundaries. These precipitated particles and  $\gamma + \gamma'$ eutectic hinder the movement of dislocations and generate many cracks during the SLM forming process. In addition, DIVYA et al [35] provided the same conclusions and determined that carbides enriched in Ti, Al, Hf, Ta, and Cr elements are metastable MC-type carbides. The IN738LC alloy undergoes the following reactions during the solidification. Discharged solute atoms form MC carbide at the grain boundary; the  $L \rightarrow \gamma + \gamma'$  eutectic reaction occurs near the end of solidification, and part of  $\gamma + \gamma'$  eutectic is formed by the constitutional liquation of MC. Furthermore, as the reaction progresses, there are various additional structures formed by small amount of other elements at grain boundaries, such as various borides, sulfides, and intermetallic compounds. These phases are formed at low temperatures and lead to an increase in the solidification temperature range [36]. Clearly, with an increase in the Zr content in the powders, Ti, Nb, Mo, W, Ta, and Zr in the superalloy are discharged into liquid phase, and a large amount of MC carbides are formed during the solidification process (Fig. 5). With the progress of the solidification reaction, part of the liquid phase is transformed into  $\gamma + \gamma'$  eutectic; simultaneously, the enrichment of Zr in solution leads to a continuous increase in the volume fraction of precipitate particles distributed at grain boundaries, and formation of solidification cracks promoted [37,38]. In addition, the cooling rate of the SLM process is faster, and there is a high vacancy concentration and dislocation density inside the alloy (Fig. 5(b)). The dislocation density of Sample 2 (0.12 wt.% Zr) at grain boundaries is considerably higher than that within the grains, and the movement of dislocations is hindered by the MC carbide particles, which generates stress concentration and finally leads to the occurrence of cracks during SLM formation [39].

#### 4.3 Tensile fractures

Figure 11 shows the fracture surface of samples with different Zr contents. Sample 1 (0.024 wt.% Zr) fractured along the 45° direction, and many dimples dispersed on this section (Fig. 11(b)). This sample exhibits better elongation and tensile strength because fine MC carbides are dispersed at the grain boundary, which pins the dislocation movement and strengthens the grain boundary (Fig. 5(a)). The fracture morphology of Sample 2 (0.12 wt.% Zr) is shown in Fig. 11(c); a flat fracture and numerous original cracks are observed. There are clear growth patterns of intact columnar crystal on the fracture surface, and typical intergranular fracture characteristics are presented (Fig. 11(d)). In addition, Sample 2 (0.12 wt.% Zr)

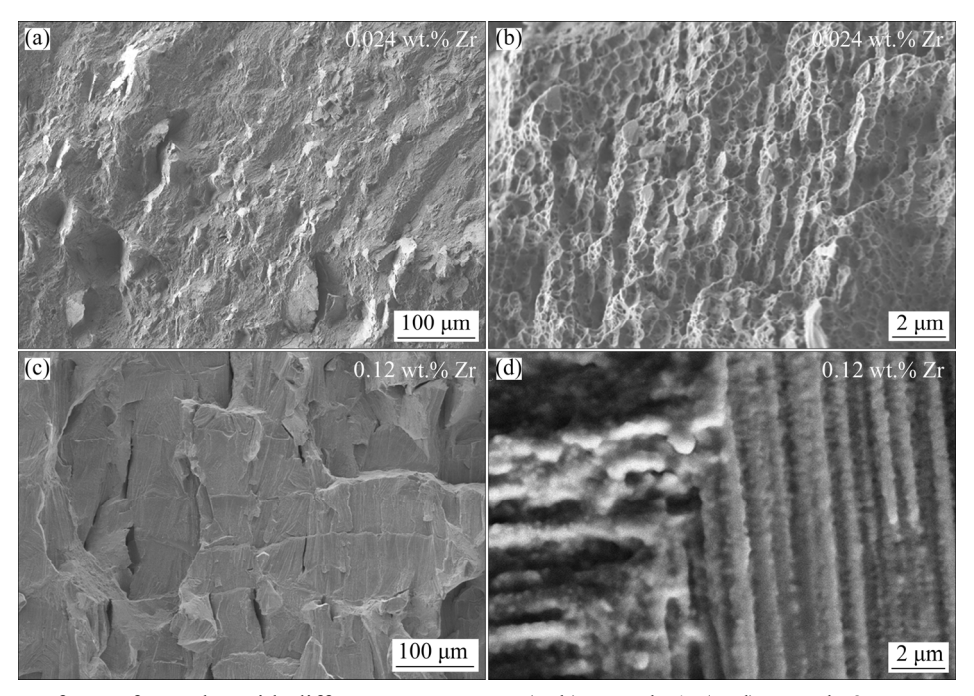


Fig. 11 Fracture surfaces of samples with different Zr contents: (a, b) Sample 1; (c, d) Sample 2

exhibits weaker mechanical properties and almost no deformation. Large-size continuous MC carbides at grain boundaries hinder the movement of dislocations and cracks, which preferentially propagate along the grain boundaries of carbides and considerably reduce mechanical properties [40].

The mechanical properties of SLM-treated parts can be improved by optimizing the process parameters, whereas the forming quality is largely affected by the combination of processing parameters and powder characteristics. The use of similar optimization parameters does not produce high quality parts because powder characteristics change; there is a matching relationship between process parameters and powder characteristics. Sample 2 (0.12 wt.% Zr) exhibits the limited improvement in mechanical properties by simply adjusting the printing strategy of interlayer angle. Subsequent to further optimization of the printing process parameters, its mechanical properties considerably increase (Fig. 8). The influence of process parameters on solidification structure and crack of high Zr content powder SLM-treated parts requires additional investigation.

#### **5 Conclusions**

(1) When the Zr content in the original powders changes from 0.024 wt.% to 0.12 wt.%,

crack density (area ratio) increases. Solidification cracks are mainly distributed at the center of the molten pool and extend to multiple layers along column grain boundaries of the epitaxially grown  $\langle 001 \rangle$  orientation.

- (2) The increased Zr content in the powders promotes the enrichment of Ti, Nb, Ta, Mo, W, Al, and Zr elements at grain boundaries, reduces the solidus temperature of the IN738LC alloy, and broadens the solidification temperature range. M(Ti,Nb,Mo,W,Zr)C carbides are continuously distributed at grain boundaries with lager size and higher quantity.
- (3) Sample 1 (0.024 wt.% Zr) exhibits the ultimate tensile strength of 1113 MPa, and the ultimate tensile strength of Sample 2 (0.12 wt.% Zr) decreases to 610 MPa. The optimization of printing parameters of Sample 2 (0.12 wt.% Zr) considerably increases the ultimate tensile strength by 55.2% to 947 MPa, and plasticity is considerably improved.

#### **Acknowledgments**

The authors are grateful for the financial supports from the Major Project of Science and Technology of Gansu Province, China (No. 17ZD2GC011), and the Hongliu First-class Discipline Construction Plan of Lanzhou University of Technology, China (No. CGZH001).

#### References

- [1] GU D D, MEINER W, WISSENBACH K, POPRAWE R. Laser additive manufacturing of metallic components: Materials, processes and mechanisms [J]. International Materials Reviews, 2015, 57(3): 133–164.
- [2] LIU Chang, WANG Chen-yu, LIU He, WANG Zhong-han, LIN Gao-yong. Mechanical properties and biocompatibility of 3D printing Ti6Al4V titanium alloy scaffolds [J]. The Chinese Journal of Nonferrous Metals, 2018, 28(4): 758–765. (in Chinese)
- [3] CHENG Ling-yu, ZHANG Sheng, WEI Qing-song, SHU Yu-sheng. Microstructure and mechanical properties of stainless steel and nano hydroxyapatite composites fabricated by selective laser melting [J]. The Chinese Journal of Nonferrous Metals, 2014, 24(6): 1510–1517. (in Chinese)
- [4] HARRISON N J, TODD I, MUMTAZ K. Reduction of micro-cracking in nickel superalloys processed by selective laser melting: A fundamental alloy design approach [J]. Acta Materialia, 2015, 94: 59–68.
- [5] XIAO W H, LU S Q, WANG Y C, SHI J. Mechanical and tribological behaviors of graphene/Inconel 718 composites [J]. Transactions of Nonferrous Metals Society of China, 2018, 28(10): 1958–1969.
- [6] DANIS Y, ARVIEU C, LACOSTE E, LARROUY T, QUENISSET J M. An investigation on thermal, metallurgical and mechanical states in weld cracking of IN738LC superalloy [J]. Materials & Design, 2010, 31(1): 402–416.
- [7] KUNZE K, ETTER T, GRÄSSLIN J, SHKLOVER V S. Texture, anisotropy in microstructure and mechanical properties of IN738LC alloy processed by selective laser melting (SLM) [J]. Materials Science and Engineering A, 2015, 620: 213–222.
- [8] ATTALLAH M M, JENNINGS R, WANG X Q, CARTER L N. Additive manufacturing of Ni-based superalloys: The outstanding issues [J]. MRS Bulletin, 2016, 41(10): 758–764.
- [9] QIU C L, CHEN H X, LIU Q, YUE S, WANG H M. On the solidification behaviour and cracking origin of a nickel-based superalloy during selective laser melting [J]. Materials Characterization, 2019, 148: 330–344.
- [10] GU H F, GONG H J, DILIP J J S, PAL D, HICKS A, DOAK H, STUCKER B. Effects of powder variation on the microstructure and tensile strength of Ti6Al4V parts fabricated by selective laser melting [C]// Proceedings of the 25th Annual International Solid Freeform Fabrication Symposium. Austin, TX, USA, 2014: 4–6.
- [11] CARTER L N, MARTIN C, WITHERS P J, ATTALLAH M M. The influence of the laser scan strategy on grain structure and cracking behaviour in SLM powder-bed fabricated nickel superalloy [J]. Journal of Alloys and Compounds, 2014, 615(2): 338–347.
- [12] CATCHPOLE-SMITH S, ABOULKHAIR N, PARRY L, TUCK C, ASHCROFT I A, CLARE A J. Fractal scan strategies for selective laser melting of 'Unweldable' nickel superalloys [J]. Additive Manufacturing, 2017, 15: 113–122.
- [13] WANG H, ZHANG X, WANG G B, SHEN J, ZHANG G Q,

- LI Y P, YAN M. Selective laser melting of the hard-to-weld IN738LC superalloy: Efforts to mitigate defects and the resultant microstructural and mechanical properties [J]. Journal of Alloys and Compounds, 2019, 807: 151662.
- [14] ENGELI R, ETTRR T, HÖVEL S, WEGENER K. Processability of different IN738LC powder batches by selective laser melting [J]. Journal of Materials Processing Technology, 2016, 229: 484–491.
- [15] TOMUS D, ROMETSCH P A, HEILMAIER M, WU X H. Effect of minor alloying elements on crack-formation characteristics of Hastelloy-X manufactured by selective laser melting [J]. Additive Manufacturing, 2017, 16: 65–72.
- [16] GUO J T. Science of superalloy material [M]. Beijing: Science Press, 2008: 136–168. (in Chinese)
- [17] OJO O A, RICHARDS N L, CHATURVEDI M C. Liquation of various phases in HAZ during welding of cast Inconel 738LC [J]. Materials Science and Technology, 2004, 20(8): 1027–1034.
- [18] MONTAZERI M, GHAINI F M. The liquation cracking behavior of IN738LC superalloy during low power Nd:YAG pulsed laser welding [J]. Materials Characterization, 2012, 67: 65–73.
- [19] HEYDARI D, SHAHKARAM FARDA A, BAKHSHI A, DREZET J M. Hot tearing in polycrystalline Ni-based IN738LC superalloy: Influence of Zr content [J]. Journal of Materials Processing Technology, 2014, 214(3): 681–687.
- [20] LIANG Y J, CHENG X, WANG H M. A new microsegregation model for rapid solidification multicomponent alloys and its application to single-crystal nickel-base superalloys of laser rapid directional solidification [J]. Acta Materialia, 2016, 118: 17–27.
- [21] CLOOTS M, UGGOWITZER P, WEGENER K. Investigations on the microstructure and crack formation of IN738LC samples processed by selective laser melting using Gaussian and doughnut profiles [J]. Materials & Design, 2016, 89: 770–784.
- ZHANG H B, XIA W Y, ZHANG S L. Relationship between microstructure and properties of Ni-base superalloy IN-738
   Journal of Iron and Steel Research, 2003, 15(7): 66-71. (in Chinese)
- [23] XU J Y, DING Y T, HU Y, GAO Y B, CHEN J J, YANG Q. Investigation on selective laser melting processing optimization and microstructure and property of Inconel 738 alloy [J]. Rare Metal Materials and Engineering, 2019, 48(11): 3727–3734. (in Chinese)
- [24] WEI H L, MAZUMDER J, DEBROY T. Evolution of solidification texture during additive manufacturing [J]. Scientific Reports, 2015, 5: 16446.
- [25] GU D D, SHI Q M, LIN K J, XI L X. Microstructure and performance evolution and underlying thermal mechanisms of Ni-based parts fabricated by selective laser melting [J]. Additive Manufacturing, 2018, 22: 265–278.
- [26] LIU J, TO A C. Quantitative texture prediction of epitaxial columnar grains in additive manufacturing using selective laser melting [J]. Additive Manufacturing, 2017, 16: 58–64.
- [27] AKRAM J, CHALAVADI P, PAL D, STUCKER B. Understanding grain evolution in additive manufacturing through modeling [J]. Additive Manufacturing, 2018, 21: 255–268.
- [28] TAO P, LI H X, HUANG B Y, HU Q D, GONG S L, XU Q Y.

- The crystal growth, intercellular spacing and microsegregation of selective laser melted Inconel 718 superalloy [J]. Vacuum, 2019, 159: 382–390.
- [29] BARTLETT J, LI X D. An overview of residual stresses in metal powder bed fusion [J]. Additive Manufacturing, 2019, 27: 131–149.
- [30] KONTIS P, CHAUVET E, PENG Z, HE J Y, SILVA A K, RAABE D, TASSIN C, BLANDIN J, ABED S, DENDIEVEL R, GAULT B, MARTIN G. Atomic-scale grain boundary engineering to overcome hot-cracking in additively manufactured superalloys [J]. Acta Materialia, 2019, 177: 209–221.
- [31] DUPONT J N, LIPPOLD J C, KISER S D. Welding metallurgy and weldability of nickel-base alloys [M]. New Jersey: John Wiley & Sons Inc, 2009: 157–254.
- [32] WOLF M, SCHOBBERT H, BÖLLINGHAUS T, HEROLD H. Hot cracking phenomena in welds [M]. Berlin Heidelberg: Springer, 2005: 245–268.
- [33] ANDERSSON J O, HELANDER T, HÖGLUND L, SHI P F, SUNDMAN B. Thermo-Calc & DICTRA, computational tools for materials science [J]. Calphad, 2002, 26(2): 273–312.
- [34] WANG X Q, CARTER L N, PANG B, ATTALLAH M M, LORETTO M H. Microstructure and yield strength of SLM-fabricated CM247LC Ni-superalloy [J]. Acta Materialia, 2017, 128: 87–95.

- [35] DIVYA V D, MORENO R M, MESSÉ O M D M, BARNARD J S, BAKER S, ILLSTON T, STONE H J. Microstructure of selective laser melted CM247LC nickel-based superalloy and its evolution through heat treatment [J]. Materials Characterization, 2016, 114: 62–74.
- [36] OJO O A, RICHARDS N L, CHATURVEDI M C. Study of the fusion zone and heat-affected zone microstructures in tungsten inert gas-welded INCONEL 738LC superalloy [J]. Metallurgical and Materials Transactions A, 2006, 37(2): 421–433.
- [37] GRODZKI J, HARTMANN N, RETTING R, AFFELDT E, SINGER R F. Effect of B, Zr, and C on hot tearing of a directionally solidified nickel-based superalloy [J]. Metallurgical and Materials Transactions A, 2016, 47(6): 2914–2926.
- [38] OJO O A, RICHARDS N L, CHATURVEDI M C. Microstructural study of weld fusion zone of TIG welded IN738LC nickel-based superalloy [J]. Scripta Materialia, 2004, 51(7): 683–688.
- [39] RAMAKRISHNAN A, DINDA G P. Direct laser metal deposition of Inconel 738 [J]. Materials Science and Engineering, 2019, 740–741: 1–13.
- [40] RAPPAZ M, JACOT A, BOETTINGER W J. Last-stage solidification of alloys: Theoretical model of dendrite-arm and grain coalescence [J]. Metallurgical and Materials Transactions A, 2003, 34(3): 467–479.

### Zr 含量对选区激光熔化 IN738LC 合金 裂纹形成及力学性能的影响

胡 勇 1,2, 杨小康 1,2, 康文江 1,2, 丁雨田 1,2, 许佳玉 1,2, 张会莹 1,2

- 1. 兰州理工大学 省部共建有色金属先进加工与再利用国家重点实验室, 兰州 730050;
  - 2. 兰州理工大学 材料科学与工程学院, 兰州 730050

摘 要:选用工业用 IN738LC 合金粉末在相同打印工艺参数下,系统研究两批次不同 Zr 含量粉末(分别为 0.024%和 0.12%,质量分数)打印件在选区激光熔化成形过程中的裂纹密度、分布、形成机理及其对力学性能的影响。结果表明: 当原始粉末中 Zr 含量从 0.024%增加到 0.12%时,裂纹密度(面积占比)在 XOY 面由 0.15%增加到 0.87%,在 XOZ 面由 0.21%增加到 1.81%;在熔池中心位置主要形成凝固裂纹,该裂纹沿外延生长的(001)取向柱晶晶界分布并扩展。样品 1(0.024% Zr)的极限抗拉强度为 1113 MPa,拉伸断口存在韧窝;当 Zr 含量增加到 0.12 wt.%时(样品 2),样品 2 的极限抗拉强度降至 610 MPa,断口存在大量原始裂纹和裸露的柱晶晶界。通过进一步优化样品 2 的打印工艺参数,其极限拉伸强度提高到 947 MPa,增幅达到 55.2%,塑性也显著增加。

关键词:选区激光熔化; IN738LC 合金; Zr 含量; 凝固裂纹; 工艺参数优化; 力学性能

(Edited by Wei-ping CHEN)